CONSTRAINING DISK PARAMETERS OF Be STARS USING NARROWBAND Hα INTERFEROMETRY WITH THE NAVY PROTOTYPE OPTICAL INTERFEROMETER

Christopher Tycner,[1,2,3] G. C. Gilbreath,[4] R. T. Zavala,[2] J. T. Armstrong,[4] J. A. Benson,[2] Arsen R. Hajian,[5] D. J. Hutter,[2] C. E. Jones,[6] T. A. Pauls,[4] and N. M. White[7]

ABSTRACT

Interferometric observations of two well-known Be stars, γ Cas and φ Per, were collected and analyzed to determine the spatial characteristics of their circumstellar regions. The observations were obtained using the Navy Prototype Optical Interferometer equipped with custom-made narrowband filters. The filters isolate the Hα emission line from the nearby continuum radiation, which results in an increased contrast between the interferometric signature due to the Hα-emitting circumstellar region and the central star. Because the narrowband filters do not significantly attenuate the continuum radiation at wavelengths 50 nm or more away from the line, the interferometric signal in the Hα channel is calibrated with respect to the continuum channels. The observations used in this study represent the highest spatial resolution measurements of the Hα-emitting regions of Be stars obtained to date. These observations allow us to demonstrate for the first time that the intensity distribution in the circumstellar region of a Be star cannot be represented by uniform disk or ringlike structures, whereas a Gaussian intensity distribution appears to be fully consistent with our observations.

Key words: stars: emission-line, Be — stars: individual (γ Cassiopeiae, φ Persei) — techniques: interferometric

1. INTRODUCTION

The application of long-baseline optical interferometry to the study of classical Be stars, although still a developing observational field, has already resulted in significant contributions to our understanding of these objects. This is in part related to the fact that the circumstellar regions associated with the closest Be stars can be spatially resolved using optical interferometers with only modest baseline lengths (10–40 m), especially if the observations are sensitive to the Hα line emission. The interferometric observations at such baselines typically yield only angular sizes of the emitting regions and in some cases also the apparent ellipticity. However, when these types of results are combined with polarimetry or spectroscopy, a number of different intrinsic properties of these regions can then be investigated or constrained.

For example, Quirrenbach et al. (1997) combined optical interferometric and spectropolarimetric observations of seven Be stars and showed that the disk orientations inferred from the two completely independent data sets agree. Furthermore, because the smallest upper limit on the disk opening angle derived by Quirrenbach et al. (1997) from the apparent ellipticity of the circumstellar region was ~20°, this was the first study that spatially resolved the circumstellar disks and supported the thin-disk paradigm for Be stars. Wood et al. (1997) constructed disk models for the Be star ζ Tau with large (tens of degrees) and small (a few degrees) disk opening angles, in which both models were consistent with the spectropolarimetry. Using the interferometric re-

sults of Quirrenbach et al. (1997), the large opening angle solution was rejected by Wood et al. (1997).

Another example of the synergy between spectroscopy and long-baseline interferometry was demonstrated by Vakili et al. (1998), in which the observations of the Be star ζ Tau at two epochs were used to detect the presence of a one-armed oscillation in the circumstellar disk. In a similar study, Berio et al. (1999) have shown that the variable asymmetric brightness distribution in the disk of γ Cas deduced from the optical interferometric data correlates with the spectral variations seen in the Hβ emission line, and these in turn can also be explained with a precessing one-armed oscillation in the equatorial disk. Although the combination of spectroscopic and interferometric observations is necessary in studies related to temporal variability, these types of data sets can also be combined to put direct constraints on the physical conditions within the circumstellar regions of Be stars. For example, Tycner et al. (2005) combined Hα emission profiles from spectroscopy with interferometric observations in Hα for a number of different Be stars and showed that there exists a direct relationship between the physical extent of the emitting region and the net Hα luminosity.

The total number of Be stars investigated with optical interferometry to date still remains quite small. This can be attributed to the relatively small number of long-baseline interferometric instruments that are sensitive to one of the strongest spectral features produced within the circumstellar disk, i.e., the Hα emission line. Even the instruments that are sensitive to the Hα emission line, or any other emission line for that matter, and have baselines long enough to spatially resolve the circumstellar regions still need to separate the signatures from the resolved disk and the unresolved (or nearly unresolved) central star that is detected at the continuum wavelengths. For this reason, it is imperative that the instrument be configured such that the contribution from the stellar photosphere to the interferometric observations at the Hα line is minimized. This can be accomplished either by sufficiently high spectral dispersion or with the use of narrowband filters.

The Navy Prototype Optical Interferometer (NPOI) is by design a multispectral instrument. However, the continuum bandpass

[1] Michelson Postdoctoral Fellow; tycner@nofs.navy.mil.
[2] US Naval Observatory, Flagstaff Station, 10391 West Naval Observatory Road, Flagstaff, AZ 86001-8521.
[3] NVI, Inc., 7257 Hanover Parkway, Suite D, Greenbelt, MD 20770.
[4] Remote Sensing Division, Code 7210, Naval Research Laboratory, 4555 Overlook Avenue SW, Washington, DC 20375.
[5] US Naval Observatory, 3450 Massachusetts Avenue NW, Washington, DC 20392-5420.
[6] Department of Physics and Astronomy, University of Western Ontario, London, ON N6A 3K7, Canada.
[7] Lowell Observatory, 1400 West Mars Hill Road, Flagstaff, AZ 86001.

1. REPORT DATE **MAY 2006**	2. REPORT TYPE **N/A**	3. DATES COVERED **-**

4. TITLE AND SUBTITLE **Constraining Disk Parameters of Be Stars Using Narrowband Hα Interferometry With the Navy Prototype Optical Interferometer**	5a. CONTRACT NUMBER
	5b. GRANT NUMBER
	5c. PROGRAM ELEMENT NUMBER
6. AUTHOR(S)	5d. PROJECT NUMBER
	5e. TASK NUMBER
	5f. WORK UNIT NUMBER

7. PERFORMING ORGANIZATION NAME(S) AND ADDRESS(ES) **U.S. Naval Observatory 3450 Massachusetts Avenue, N.W. Washington, DC 20392-5420**	8. PERFORMING ORGANIZATION REPORT NUMBER

9. SPONSORING/MONITORING AGENCY NAME(S) AND ADDRESS(ES)	10. SPONSOR/MONITOR'S ACRONYM(S)
	11. SPONSOR/MONITOR'S REPORT NUMBER(S)

12. DISTRIBUTION/AVAILABILITY STATEMENT
Approved for public release, distribution unlimited

13. SUPPLEMENTARY NOTES
The original document contains color images.

14. ABSTRACT

15. SUBJECT TERMS

16. SECURITY CLASSIFICATION OF:			17. LIMITATION OF ABSTRACT	18. NUMBER OF PAGES	19a. NAME OF RESPONSIBLE PERSON
a. REPORT **unclassified**	b. ABSTRACT **unclassified**	c. THIS PAGE **unclassified**	**SAR**	**12**	

recorded by the instrument in the Hα region, as defined by the spectral channel characteristics, can be too wide for sources with weak Hα emission. Therefore, as part of a proof of concept, we equipped the NPOI with a set of custom narrowband filters[8] centered on the Hα line to further decrease the stellar contribution at the continuum wavelengths in that channel (Pauls et al. 2001). These initial observations demonstrated that, with only small modifications to our current instrumental configuration, interferometric observations of Be stars can be obtained with the narrowband filters.

In this paper we demonstrate the quantitative results based on the narrowband interferometric observations of two stars known for their relatively strong Hα emission, γ Cassiopeiae (HR 264) and φ Persei (HR 496). Because the circumstellar regions of both stars were resolved by long-baseline interferometry in the past, they are suitable targets for direct comparison of the results produced by the new observational setup with those already presented in the literature (Quirrenbach et al. 1997; Tycner et al. 2003). Also, the interferometric observations presented in this study represent some of the highest spatial resolution measurements of the Hα-emitting regions obtained to date. This allows us to test the various models for intensity distribution at high enough spatial frequencies that the degeneracy between the various models is eliminated.

2. OBSERVATIONAL SETUP

The NPOI consists of four stationary astrometric stations and a Y-shaped imaging station configuration in which movable siderostat elements can be repositioned (see the description of the instrument by Armstrong et al. 1998). Currently, two movable stations are operational. The goal is to have six movable stations that will allow simultaneous observations with up to six reconfigurable elements. Although the successful combination of light from six stations has already been demonstrated with the NPOI (Hummel et al. 2003), at the time of the observations presented in this paper only four stations were available for observations. These four stations gave access to baselines with lengths in the range of 18.9–64.4 m, as shown schematically in Figure 1.

The instrument was designed to accept stellar light from up to six siderostats simultaneously, in which each element sends a 12 cm light beam through vacuum pipes to the beam combiner lab. At the beam combiner, the light beams are split and recombined in such a way that the interference fringes between all siderostat pairs (for a total of 15 unique pairs) are constructed. Figure 2 illustrates the propagation of light for six input beams. The three output beams that are intercepted are dispersed by a set of three prisms onto individual lenslet arrays, which in turn are fiber-coupled to a cluster of photon-counting avalanche photodiodes. Each fiber corresponds to a single channel with spectral characteristics set by the position of the lenslet array and the physical width of a single lenslet along the dispersion direction.

The spectra of Be stars show many spectral lines in emission. For example, in the 510–880 nm region covered by our interferometric observations, emission lines of elements such as H I, He I, O I, Si II, and Fe II can be detected. However, except for hydrogen lines all of the emission lines are very weak, having equivalent widths (EWs) of ≲0.1 nm, and therefore are lost in the continuum signal present in each spectral channel (the widths of the spectral channels range from 10 to 26 nm). Even in the case of the hydrogen lines present in our spectral region of interest, only the Hα line has a large enough EW to contribute a detect-
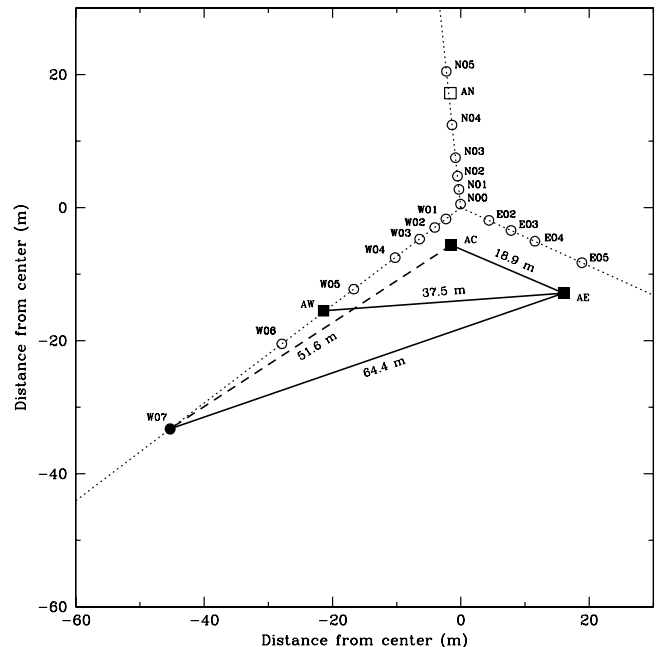

FIG. 1.—Schematic of the inner portion of the NPOI array. The imaging (*circles*) and astrometric (*squares*) stations used in the Hα observations presented in this paper are shown with filled symbols. Baselines that could be recorded on two out of three outputs from the beam combiner are also shown with their respective physical lengths indicated. The baseline that was not accessible to observations of γ Cas due to sky coverage limitation is shown with the dashed line.

able interferometric signal in the Hα-containing channel. Therefore, for the purpose of the Hα observations, the lenslet array is aligned such that the emission line is centered on a single channel that has a spectral width of 15 nm. Because the typical EWs of Hα emission lines in Be stars are usually not more than 4 nm (see, e.g., Table 6 in Tycner et al. 2005), the contribution from the circumstellar region to the net signal is typically less than 25%. For sources with very weak emission, the fractional contribution to the net signal can be much less than the magnitude of the random and systematic uncertainties, which are typically at the few percent level.

To increase the contrast between the interferometric signatures from the Hα-emitting circumstellar region and the central star, we have inserted a narrowband filter at each of the three outputs from the beam combiner (see Fig. 2). These filters have a high transmission (~90%) in a 2.8 nm region centered on the Hα line, which suppresses the nearby continuum emission but does not significantly attenuate radiation outside a ~100 nm region centered at the line. Because we need to detect the interferometric signal outside of the spectral channel containing the Hα emission for both calibration and fringe tracking purposes, the filter has high enough transmission in the 500–600 and 710–850 nm regions that the continuum channels are still usable. The transmission curve of the custom-made filter is shown in Figure 3 along with the superposed locations of the spectral channels that were used to record the fringe signals.

In the current instrumental setup the signals from up to 32 channels can be recorded simultaneously by the NPOI electronics. Because these channels are divided equally between two output beams from the beam combiner, data from one of the three output beams are currently not recorded (recall Fig. 2). This results in interferometric observations that do not sample all the baseline configurations that are possible with a given set of elements, as shown in Figure 1. Furthermore, because the long-delay lines are

---

[8] The custom Hα filters were manufactured by David E. Upton of Omega Optical, Brattleboro, VT 05301.

Output Beams

1,2,4,5 to lenslet array # 3
(Output not recorded)

1,3,4,6 to lenslet array # 2
(AE-AW)

2,3,5,6 to lenslet array # 1
(AE-AC),(AC-W7),(AE-W7)

Filters Prisms

Mirrors

Beamsplitter

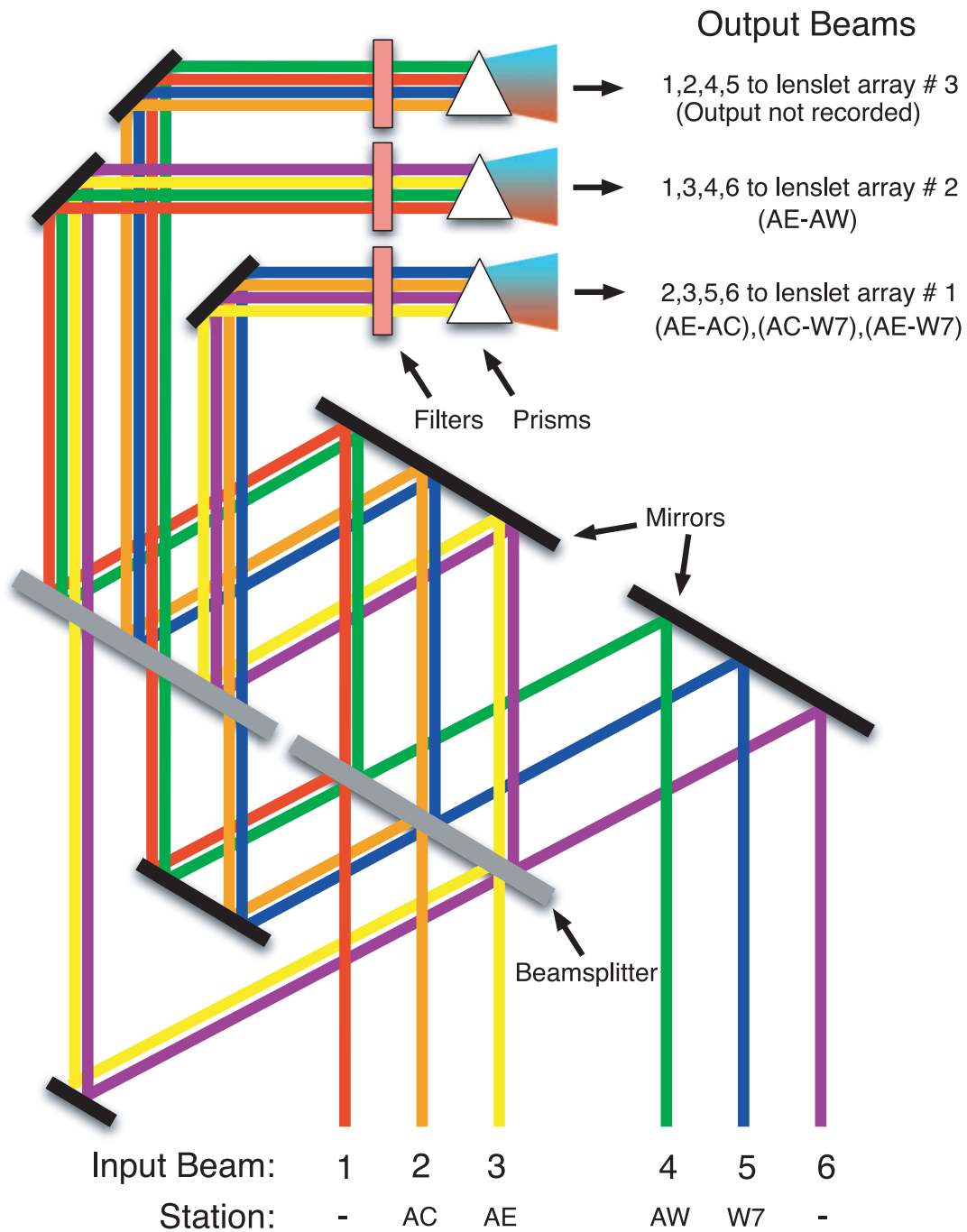| Input Beam:	1	2	3		4	5	6
Station:	-	AC	AE		AW	W7	-

Fig. 2.—Schematic of the beam combiner illustrating the propagation of light from up to six input beams. The three output beams that are intercepted by the pick-off optics sample all available baseline configurations (up to 15 element pairs with six input beams).

not implemented yet, the maximum path difference that can be introduced between a pair of siderostats (to compensate for the different distances between each station and the star) is currently 35 m, and this results in restricted ranges of declination and hour angle over which a star can be observed at a given baseline. For example, Figure 4 shows the accessible sky coverage for three different configurations; in one case all four elements (AC, AW, AE, and W7) are used, and in the other two configurations either the AC or the W7 station is excluded. Therefore, for γ Cas the observations utilizing the AC-W7 baseline are not currently possible, whereas for ϕ Per, which is $10°$ lower in the sky, such observations are possible. Of course, with the expected implementation of the long-delay lines, optical path difference compensa-

tion of up to $\sim$400 m will become possible, and the accessible sky coverage will be significantly less restricted.

3. OBSERVATIONS

3.1. *Interferometry*

The typical NPOI observing and data reduction procedures are described in Hummel et al. (2003). Here we provide a brief review of the process. During a 30 s observation fringe data are recorded every 2 ms. The squared visibility (V^2) estimators from the 2 ms data are averaged on 1 s intervals, and the 1 s data points are processed using a suite of custom reduction software. Outlier points are flagged on the basis of the residuals of the delay,
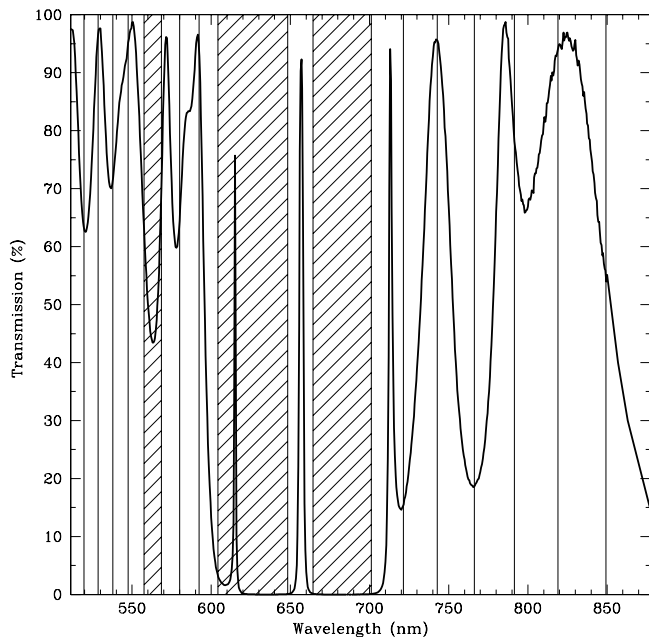
FIG. 3.—Transmission curve for the Hα filter in the spectral region covered by the 16 channels that were used to record the interferometric signals. The edges of the spectral channels are marked with vertical lines, and the spectral regions for which the signals were not recorded are shown with hatched regions.
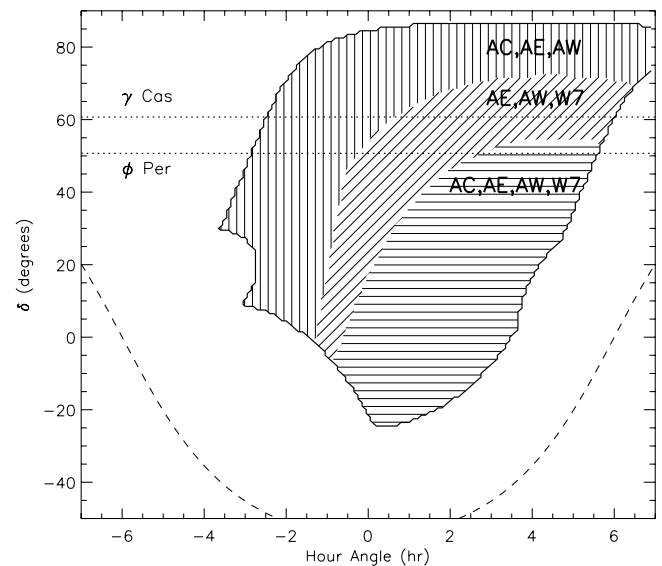

FIG. 4.—Accessible sky coverage for interferometric observations using different combinations of the array elements. At a fixed declination, the largest accessible hour angle (HA) range is determined by the limits imposed on the siderostats motion (to the east) and on a typical zenith angle limit of $60°$ (to the west). The accessible HA range is further constrained by limitations imposed by optical path compensation components. The smallest area (*horizontal hatched region*) corresponds to observations at all four stations (AC, AE, AW, and W7), which have a declination limit of $55°$. The declination limit, as well as the sky coverage, can be increased by excluding the AC (*diagonal hatched region*) or the W7 station (*vertical hatched region*). The positions of the horizon (*dashed line*), φ Per, and γ Cas (*dotted lines*) are also indicated.

seeing indicators, photon rates, and squared visibilities. Finally, depending on how many 1 s data points have been flagged as bad, up to 30 points are averaged to produce a single squared visibility measure for each 30 s interval, also known as a "scan." Typically, following a procedure similar to that used in obtaining the V^2 data, the closure phase and triple amplitude can also be obtained for each scan. However, because these quantities were not obtained for the data presented in this paper, we do not include them in our discussion.

The V^2 value for a single scan is obtained in the same way for both the target and the calibrator star, as well as for the incoherent scans (also known as the "off-the-fringe scans"). The typical observational sequence consists of a pair of coherent and incoherent scans on a target followed by the same pair of scans on a calibrator. The procedure is repeated for as long as the scans of the target star are acquired. The incoherent scans are necessary to estimate the additive bias terms affecting the squared visibility measures (see Hummel et al. 2003 for more details). The bias term is a squared visibility measure that one obtains in the case of a completely incoherent signal, which for an ideal system should be exactly zero. Because the calibration procedure removes multiplicative effects, the subtraction of the additive bias term must be performed before calibration corrections are applied. We remove the bias terms from the squared visibilities of both the target and the calibrator stars following the method described in Wittkowski et al. (2001) and Hummel et al. (2003).

As we have discussed in § 2, γ Cas could not be observed on the AC-W7 baseline because its high declination places the star outside the accessible sky coverage (defined by the limits imposed by the optical path compensation components). Having slightly lower declination, φ Per was not constrained by the same limitation. Because the two stars are separated in right ascension by less than 50 minutes, it was more efficient to observe both stars in the same mode (i.e., using only three stations). The loss of one station for φ Per was compensated for by the extended hour angle range over which it was possible to observe this star (recall Fig. 4). Another advantage of having only one baseline on

each spectrograph is the elimination of multibaseline cross-talk effects that may be present in the data (Schmitt et al. 2005). The disadvantage of having only two simultaneous baselines is that some interferometric observables, such as closure phase and triple amplitude, could not be obtained because they require at least three simultaneous baselines.

We observed γ Cas and φ Per during 2004 November and December. Although we lost many nights due to poor weather, we still managed to obtain ∼100 scans for each star with almost all the scans providing data on two baselines. Table 1 shows a log of the observations. On 2004 December 8 the vacuum pipes between the sixth and seventh station on each of the three arms were disconnected (see Fig. 1 for the layout of the imaging array) in order to install safety vacuum valves. This resulted in the W7 station being unavailable for observations starting 2004 December 10, and therefore, only observations utilizing the AE, AC, and AW stations were recorded for the rest of the observing run. On 2004 December 2 we temporarily removed the narrowband filters from the outputs of the beam combiner to obtain observations without the use of the filters but with the same instrumental configuration.

For the purpose of the analysis presented in this paper, we are only interested in the squared visibilities from the spectral channels that contain the Hα emission line. However, before these V^2 values can be extracted from the observational data set, we need to calibrate these quantities. We follow the calibration procedure outlined in Tycner et al. (2003), which we only summarize here. The calibration procedure uses the continuum channels at a given scan and baseline to estimate a correction function that has a quadratic dependence in λ^{-1}, which is then applied to the squared visibility measure in the spectral channel that contains the Hα emission line. Because the correction function is a slowly varying function across channels, it cannot account for any high-order channel-to-channel variations. Therefore, in the current analysis we estimated the V^2 amplitudes of the high-order variations across

	γ Cas (Number of Scans)			φ Per (Number of Scans)		
UT Date	AE-AC	AE-W7	AE-AW	AE-AC	AE-W7	AE-AW
2004 Nov 3	...	2	2	...	2	2
2004 Nov 4	...	7	7	...	9	9
2004 Nov 5	...	7	7	...	8	8
2004 Nov 30	...	...	5	...	...	6
2004 Dec 1	...	2	2	...	8	8
2004 Dec 2[a]	...	9	9	...	14	14
2004 Dec 3	...	10	10	...	7	7
2004 Dec 4	...	3	6	...	3	6
2004 Dec 10	9	...	9	9	...	9
2004 Dec 11	11	...	11	12	...	12
2004 Dec 12	8	...	9	11	...	11
2004 Dec 19	9	...	9	9	...	10
2004 Dec 23	12	...	12	10	...	10
Total	49	40	98	51	51	112

Note.—The AC-W7 baseline was not accessible to γ Cas (see § 3.1), and therefore the AC station was not used until after 2004 December 4, when the W7 station came offline due to gate valve work.
[a] The narrowband Hα filter was not used on 2004 December 2.

the spectral channels using the residuals that could not be removed with the quadratic polynomials from the scans of the calibrator stars. The calibrators used for γ Cas and φ Per were ε Cas (HR 542) and ζ Cas (HR 153), respectively. Both calibrators are B-type stars and were verified by spectroscopic observations to have Hα in absorption. After confirming that the channel-to-channel variations established based on observations of the calibrators are stable on timescales longer than one night, we calculated nightly averages that were then divided out of the scans of the target stars.

After applying the bias and the calibration corrections to all scans, we extracted the squared visibilities for the Hα channel forming two large data sets, one for γ Cas (with 169 data points)

and the other for φ Per (with 186 data points). The observations obtained on 2004 December 2, when the narrowband filters were not used, are treated as separate data sets. Figures 5 and 6 show the resulting (u, v)-plane coverage at the AC-AE, AE-AW, and AE-W7 baselines in the Hα channel for γ Cas and φ Per, respectively. The corresponding V^2 data for the two stars are shown in Figures 7 and 8 for observations obtained with the narrowband filter, whereas the V^2 observations obtained without the filters are shown in Figures 9 and 10.

3.2. Spectroscopy

The interferometric observations obtained with the NPOI do not contain enough spectral information to help us establish the properties of the Hα emission line. Therefore, we observed γ Cas and φ Per using a fiber-fed echelle spectrograph (also known as
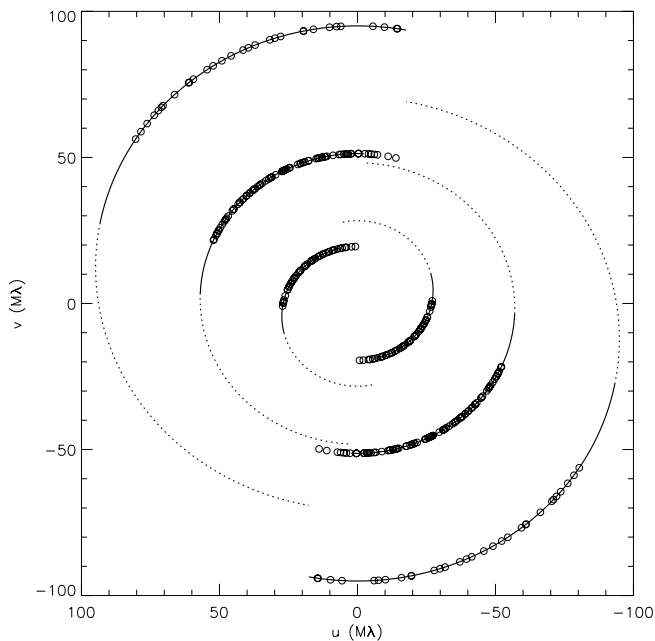

Fig. 5.—Sampling of the (u, v)-plane by the Hα observations of γ Cas on three baselines with lengths of 18.9 (AC-AE), 37.5 (AE-AW), and 64.4 m (AE-W7). For comparison, sample coverages (not limited by the HA limitations shown in Fig. 4) over 6 hr ranges in HA from the meridian to the east (*dotted line*) and to the west (*solid line*) are also shown.
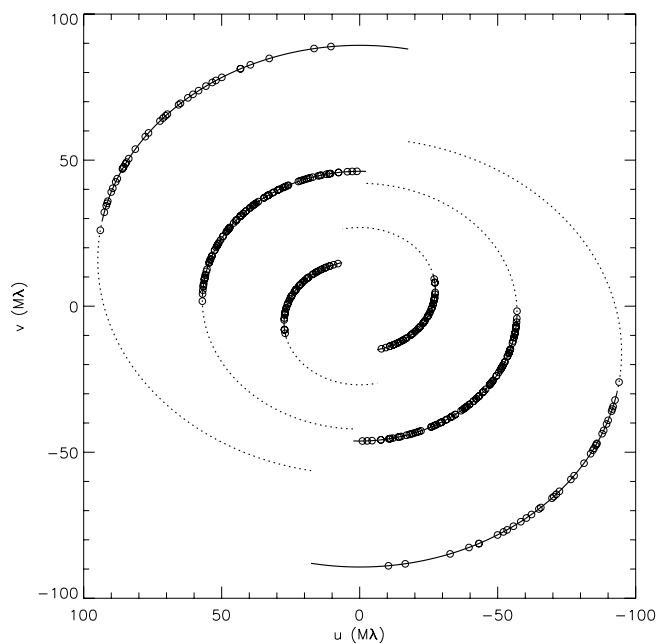

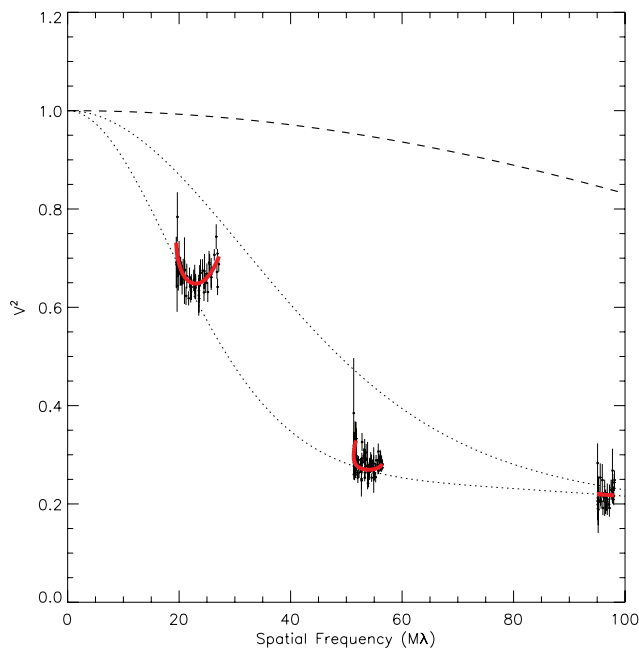Fig. 6.—Same as Fig. 5, but for the (u, v)-plane coverage of φ Per.

Fig. 7.—Calibrated squared visibilities from the Hα channel of γ Cas obtained at three baselines. The elliptical Gaussian model (*red solid line*) fitted to all observations is shown at each baseline for the same HA range as defined by the observations. The model contains a contribution from the stellar photospheric disk (*dashed line*) that is modeled with eq. (2). Model curves evaluated at the minor (*top dotted line*) and major (*bottom dotted line*) axes of the elliptical Gaussian model are also shown.

the Solar-Stellar Spectrograph [SSS]), which is located at the Lowell Observatory's John S. Hall 1.1 m telescope. The SSS instrument produces spectra in the Hα region with a resolving power of ∼10,000 and a signal-to-noise ratio (S/N) of a few hundred in the Hα region. The SSS observations were reduced using standard reduction routines written in IDL[9] (Hall et al. 1994), and the

---

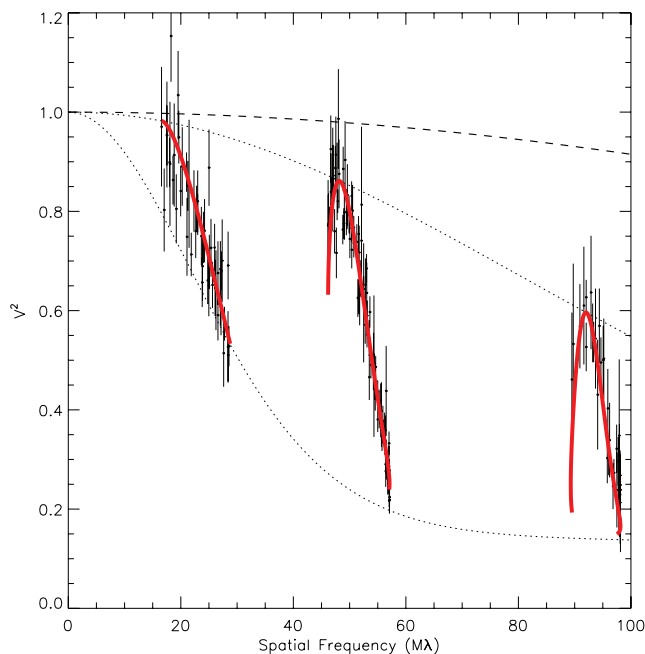[9] Interactive Data Language of RSI, ITT Industries, Boulder, CO 80301.

Fig. 8.—Same as Fig. 7, but for the Hα observations of φ Per.
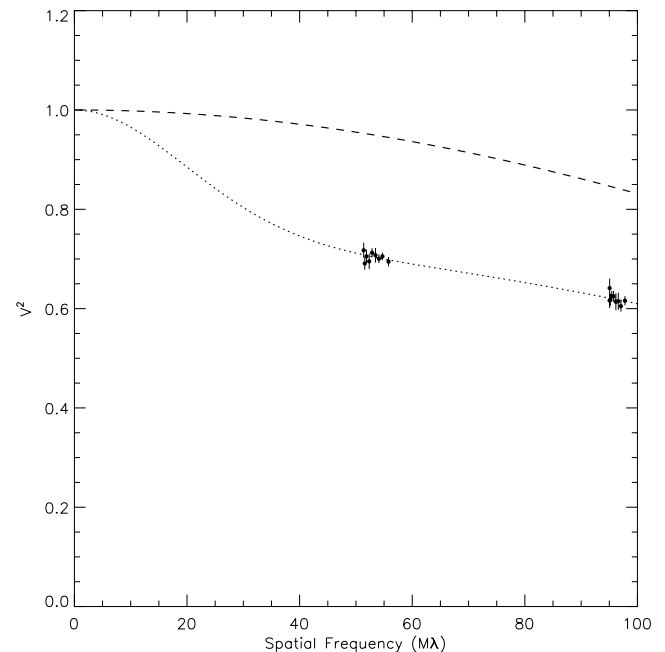

Fig. 9.—Calibrated squared visibilities from the Hα channel of γ Cas obtained on 2004 December 2 without the use of a narrowband filter at two baselines (AE-AW and AE-W7). The best-fit circularly symmetric Gaussian model (*dotted line*) and the stellar photospheric disk (*dashed line*) are also shown.

resulting Hα profiles of γ Cas and φ Per are shown in Figures 11 and 12, respectively.

The Hα emission of γ Cas is known to be stable on timescales greater than 1 yr, and our spectra confirm this. The EWs of the four Hα profiles shown in Figure 11 range from −3.0 to −3.2 nm. Because the largest uncertainty associated with these values is the precision of continuum normalization, which we estimate at 3%, for the purpose of our study we use an EW of −3.1 ± 0.1 nm for the Hα emission of γ Cas.
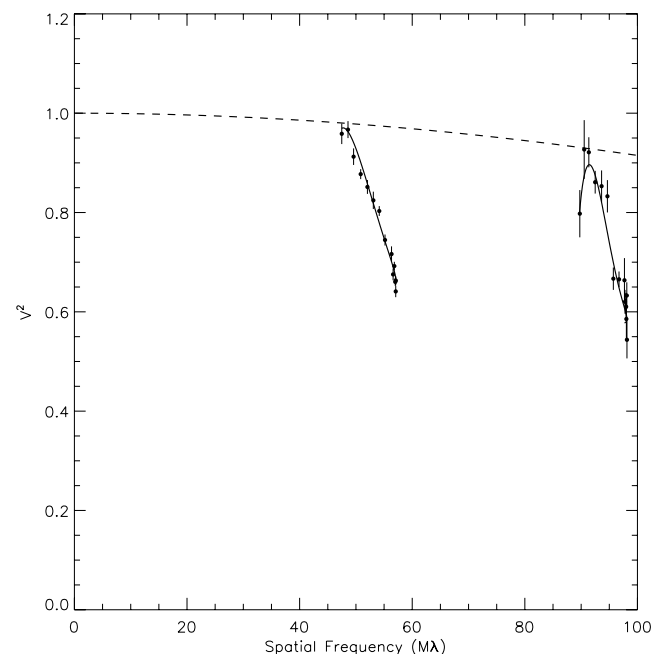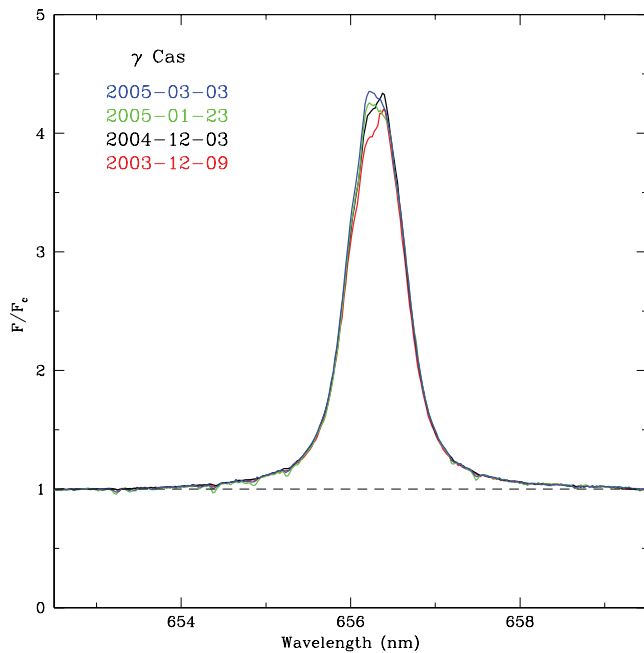

Fig. 10.—Same as Fig. 9, but for the Hα observations of φ Per with the best-fit elliptical Gaussian model shown (*solid lines*).

FIG. 11.—Hα profiles of γ Cas obtained at four different epochs.

FIG. 12.—Hα profiles of φ Per obtained at three different epochs.

As we discuss in § 5.3, φ Per is a Be+sdO spectroscopic binary with a period of 127 days and is known to show Hα variability. The observed variability is attributed in part to the radiative effects of the hot secondary on the circumstellar region associated with the primary. Although our temporal coverage is limited, we confirm the presence of Hα emission variability in φ Per. The EWs of the three profiles shown in Figure 12 are −3.8, −4.2, and −3.6 nm, which were obtained on 2004 December 3, 2005 March 3, and 2005 April 1, respectively. However, because the relative shape of the Hα profile does not appear to change significantly, we conclude that combining all of the interferometric observations from our observing run should not result in any significant errors (we return to this point in § 4.2). For this reason we adopt an Hα EW for φ Per of −3.9 ± 0.3 nm, in which the larger uncertainty should account for the intrinsic variability during our interferometric run.
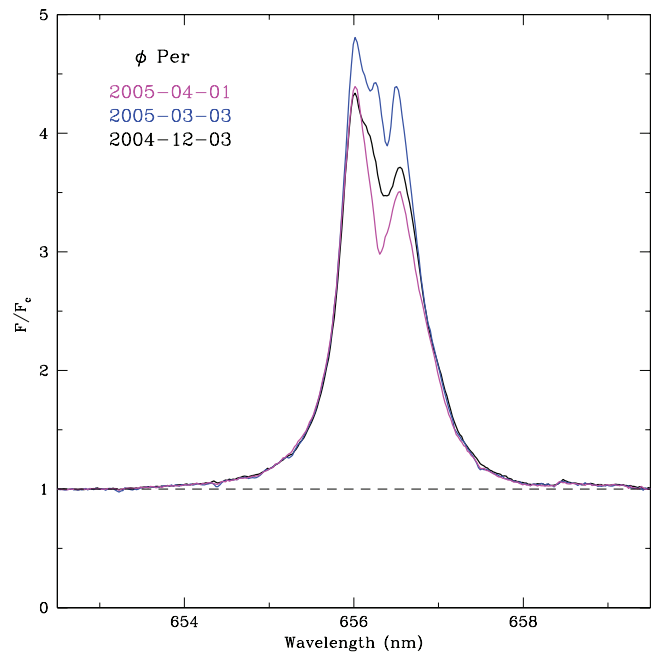
4. THE ANALYSIS

4.1. Models

The squared visibilities from the spectral channels containing the Hα emission contain two signatures, one due to the central star and the other due to the circumstellar region. Therefore, these data must be modeled with a two-component model of the form

$$V_{model}^2 = \left[c_p V_p + (1 - c_p)V_{env}\right]^2, \quad (1)$$

where V_p and V_{env} are the visibility functions representing the photosphere of the central star and the circumstellar envelope, respectively, and c_p is the fractional contribution from the stellar photosphere to the total flux in the Hα channel. Generally, both V_p and V_{env} can be complex functions, but because the models we consider in this analysis are all point-symmetric, as well as concentric, the functions are real and can be treated as visibility amplitudes.

To decrease the number of free parameters in our models we treat the angular diameter of the central star as a known quantity. This is also supported by the fact that the central stars are not significantly resolved even at our longest baseline. Furthermore,

as we discussed in Tycner et al. (2004), our best-fit models describing the Hα-emitting regions are not very sensitive to the assumed diameter of the central star (changing the diameter by a factor of 2 results in ∼1% change in the best-fit disk parameters). For the same reason we can also ignore any effects related to the rapid rotation for which Be stars are well known, because the geometric distortion and gravity darkening near the stellar equator only weakly affect our best-fit disk parameters.

The most widely used approach for predicting a stellar angular diameter is to use empirically established relationships between the stellar color index and the surface brightness, which in turn is related to the angular size (Barnes et al. 1978; van Belle 1999). Another approach would be to use tabulations of linear stellar diameters as a function of spectral class (Underhill et al. 1979). However, because there is an intrinsic scatter in stellar diameters at each spectral class and the distance to the source needs to be known to convert the linear diameter to the angular size needed for interferometry, this is not the preferred approach. Therefore, for γ Cas and φ Per we adopt the same stellar angular diameters that were used by Quirrenbach et al. (1997), which were derived using the photometric relations of Barnes et al. (1978). The angular diameters we adopt for γ Cas and φ Per are 0.56 and 0.39 mas, respectively.

We model the stellar photosphere of each star with a circularly symmetric uniform disk brightness distribution. This ensures that the central star is modeled in exactly the same way, at the continuum channels during the calibration procedure (see Tycner et al. 2003 for more details) and at the Hα channel via equation (1). Therefore, we represent the visibility function of the photospheric component of an angular diameter a with

$$V_p(u,\ v) = 2\frac{J_1(\pi a\sqrt{u^2 + v^2})}{\pi a\sqrt{u^2 + v^2}}, \quad (2)$$

where J_1 is a first-order Bessel function and u and v are the spatial frequencies, which are given by the east-west and south-north components of the projected baseline on the plane of the sky

TABLE 2
BEST-FIT MODEL PARAMETERS FOR γ Cas AND ϕ Per

Model	θ (mas)	ϵ	r	ϕ (deg)	c_p	χ_ν^2
			γ Cas			
UD............................	4.72 ± 0.03	...	0.89 ± 0.02	29.6 ± 2.5	0.53 ± 0.01	6.0
UD*	6.49 ± 0.06	...	0.52 ± 0.03	34.7 ± 1.5	0.59 ± 0.01	1.6
UR............................	7.91 ± 0.09	$0.04-0.90$	0.58 ± 0.03	$5-40$	0.58 ± 0.13	5.7
UR*	5.60 ± 0.53	0.77 ± 0.16	0.52 ± 0.03	36.0 ± 1.5	0.67 ± 0.01	1.7
GD............................	3.59 ± 0.04	...	0.58 ± 0.03	31.2 ± 1.2	0.51 ± 0.01	1.4
GD*	3.64 ± 0.05	...	0.56 ± 0.03	30.6 ± 1.4	0.51 ± 0.01	1.4
			ϕ Per			
UD............................	5.43 ± 0.13	...	0.27 ± 0.01	-61.5 ± 0.6	0.52 ± 0.01	1.4
UR............................	5.23 ± 0.33	0.58 ± 0.12	0.26 ± 0.01	-61.7 ± 0.6	0.62 ± 0.01	1.4
GD............................	2.89 ± 0.09	...	0.27 ± 0.01	-61.5 ± 0.6	0.39 ± 0.02	1.4

NOTES.—For the UD and UR models θ corresponds to the angular diameter of the major axis, and for the GD model it corresponds to the FWHM of the major axis of the elliptical Gaussian. Asterisks denote models fitted to data from the shortest two baselines only.

divided by wavelength (see § 4.1 in Thompson et al. [2001] for the definition of the [u, v]-plane).

Our interferometric observations were obtained at high spatial frequencies (i.e., at high spatial resolution), and therefore, we can compare different models of brightness distribution. Previously published work on disk models of Be stars has demonstrated that the thermal structure of the circumstellar disks can be quite complex (Millar & Marlborough 1998; Millar et al. 2000; Carciofi & Bjorkman 2006). However, for this first investigation with this new observational technique we choose to model our data with three simple models: a uniform disk (UD), a uniform ring (UR), and a Gaussian distribution (GD). The visibility amplitudes for all three models can be written as

$$V_{\rm env} = \begin{cases} \dfrac{2J_1(\pi\theta_{\rm UD}s)}{\pi\theta_{\rm UD}s}, & \text{UD}, \\[2ex] 2(1-\epsilon^2)^{-1}\left[\dfrac{J_1(\pi\theta_{\rm UR}s)}{\pi\theta_{\rm UR}s} - \dfrac{\epsilon^2 J_1(\pi\epsilon\theta_{\rm UR}s)}{\pi\epsilon\theta_{\rm UR}s}\right], & \text{UR}, \quad (3) \\[2ex] \exp\left[-\dfrac{(\pi\theta_{\rm GD}s)^2}{4\ln 2}\right], & \text{GD}, \end{cases}$$

where $\theta_{\rm UD}$ and $\theta_{\rm UR}$ correspond to the angular diameters of the UD and UR models, respectively, and $\theta_{\rm GD}$ corresponds to the full width at half-maximum (FWHM) of the Gaussian model. Because we allow all three models to have elliptical distribution on the sky, all of the above diameters describe the dimensions along the major axis. The other variables in equation (3) are ϵ, which describes the inner diameter of the ring model along the major axis (in units of $\theta_{\rm UR}$), and s, which is given by

$$s = \sqrt{r^2(u\cos\phi - v\sin\phi)^2 + (u\sin\phi + v\cos\phi)^2}, \quad (4)$$

where r is the axial ratio and ϕ is the position angle (P.A.; measured east from north) of the major axis (when $0 \leq r < 1$). For circularly symmetric structures ($r = 1$), equation (4) reduces to a simple expression for a radial spatial frequency in the (u, v)-plane given by $(u^2 + v^2)^{1/2}$.

4.2. Model Fitting

To obtain a best fit for each of the three models, we used a nonlinear least-squares IDL procedure based on the Levenberg-Marquardt method (Press et al. 1992). Each model is represented by equation (1), with the appropriate expression for the envelope component from equation (3), and a fixed visibility function for the photospheric component (eq. [2] with a fixed stellar diameter a). Therefore, the UD and GD models have four free parameters, c_p, θ, r, and ϕ, whereas the UR model has ϵ as an extra parameter. Table 2 lists the best-fit values for the parameters for all three models along with the reduced χ^2 values. By inspecting the reduced χ^2 values in Table 2 for the three γ Cas models, it is evident that the UD and UR models cannot represent the observations obtained at all three baselines. Therefore, we have also fitted models to observations of γ Cas from the shortest two baselines only, at which all three models yield similar quality fits (these models are also listed in Table 2). To check for any possible variations in the models that could be attributed to the temporal variability of our sources (especially in the case of ϕ Per), we fitted models to various subsets of our large data set. Although typically the uncertainties of the best-fit parameters are larger for models fitted to smaller data sets, all results were consistent with our solutions based on all observations.

To illustrate why the UD and UR models fail to represent the observations of γ Cas obtained at all three baselines, in Figure 13 we plot the best-fit UD, UR, and GD models, which were only fitted to data from the shortest two baselines. Each baseline provides data over a different spatial frequency range (because of different physical lengths), and these ranges are marked with thick solid lines in Figure 13. A small fraction of each range corresponds to an instant at which the projected baseline on the sky was oriented along the major axis for which these model curves were evaluated. The model curves demonstrate the inherent degeneracy present between the three models at low spatial frequencies (i.e., at low spatial resolutions the three models look the same). However, the longest baseline provides data at high enough spatial frequencies that the degeneracy between the three models is eliminated (see also Fig. 7). We conclude that the UD and UR models are inconsistent with the data obtained at the longest baseline (largest spatial frequencies), whereas the GD models fit the observations at all baselines.

The observations of ϕ Per are more challenging because the angular size of its circumstellar region is smaller than for γ Cas, and the projected baselines on the plane of the sky are not oriented along its major axis. This results in interferometric observations that do not resolve the region sufficiently well to break
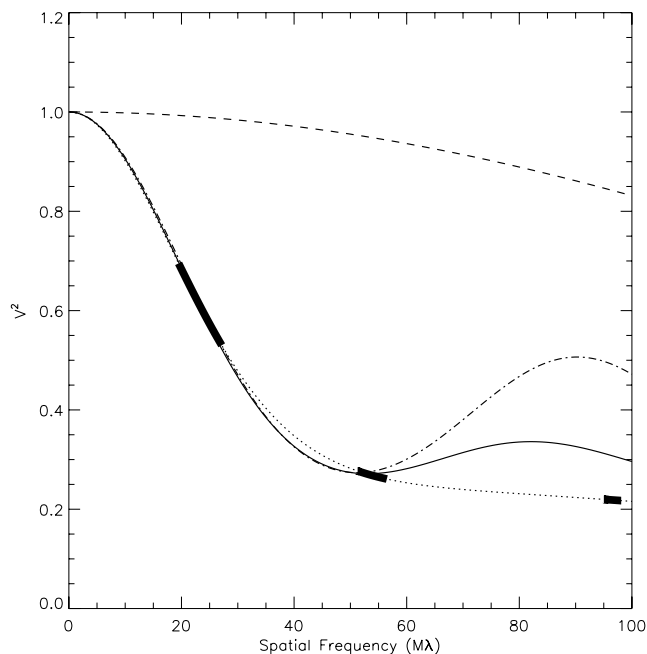
Fig. 13.—Model squared visibilities for the uniform disk (*solid line*), ring (*dash-dotted line*), and Gaussian (*dotted line*) models of γ Cas. All three models contain a contribution from a central star (*dashed line*), which is modeled using eq. (2), and are evaluated along their major axes (i.e., along their largest angular extent). The spatial frequency ranges sampled by the three baselines are indicated with thick solid lines. The models shown were fitted to the data at the two shortest baselines only.

Fig. 14.—Same as Fig. 13, but for models based on observations of ϕ Per and evaluated at three different orientations with respect to the major axis. The three families of curves correspond to 100% (*bottom three curves*), 50% (*middle three overlapping curves*), and 27% (*top three overlapping curves*) of the size of the major axis. Because the observations do not sample the disk along the major axis, the spatial frequency ranges sampled by the three baselines are indicated only along the minor axis and where the extent is 50% of the major axis (*thick solid lines*).

the degeneracy between the different models. This is also the reason that all three models for ϕ Per listed in Table 2 yield the same χ_ν^2 values. Figure 14 demonstrates the differences between the model curves based on the three best-fit models evaluated at three different projections. The three projections were chosen to correspond to the minor axis (that is, 27% of the major axis), to a direction with an extent of 50% of the major axis, and to the major axis. Because we do not have observations that resolve the major axis (recall Fig. 8), the spatial frequency ranges over which we have data are marked only on the curves that correspond to the minor axis and 50% of the major (Fig. 14, *thick solid lines*). Based on Figure 14 we conclude that in order to break the degeneracy between the models, observations either at higher spatial frequencies or along the major axis are required (as demonstrated in the case of γ Cas).

4.3. *Gaussian Distribution*

For ϕ Per we cannot exclude the UD and UR models in favor of the GD model based on interferometric data alone; however, we can demonstrate that the GD model is the preferred solution. This is because the three models that fit the ϕ Per data equally well have different best-fit values for the c_p parameter, which can be constrained by spectroscopy. For example, if the EW of the continuum flux from the star in the Hα channel is F_* (which has units of length) and the EW of the net Hα emission is $E_{H\alpha}$, then the fractional photospheric contribution in the absence of a narrowband filter (c_p^*) can be expressed as

$$c_p^* = \frac{F_*}{F_* + E_{H\alpha}}. \tag{5}$$

With the narrowband filter, F_* gets reduced to tF_*, where t is the fractional transmission in the Hα channel. The Hα emission gets reduced by the filter as well, but because the Hα emission lines
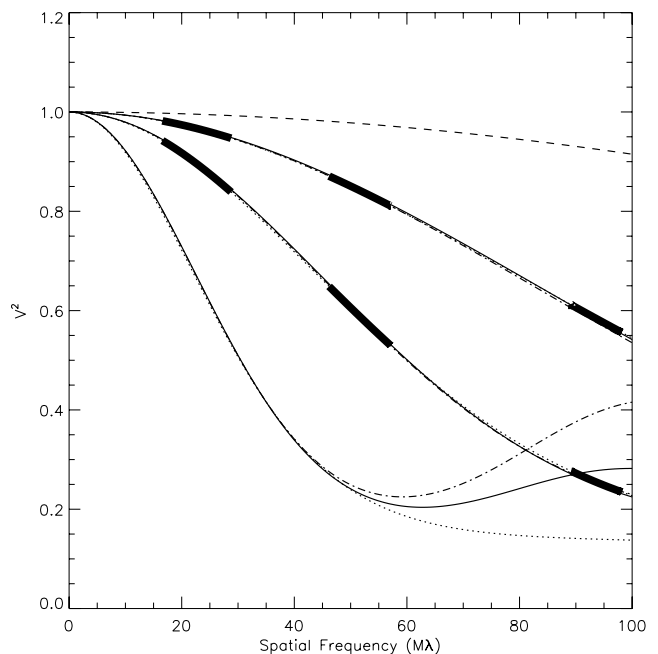
have FWHM $\lesssim 1$ nm, which is less than the width of 2.8 nm of the narrowband region, we can approximate the transmission at the Hα line (η) by the peak transmission of 92% of the narrowband region (recall Fig. 3). Therefore, the c_p parameter for the case including the filter can be written as

$$c_p = \frac{tF_*}{tF_* + \eta E_{H\alpha}}. \tag{6}$$

Taking the ratio of equations (5) and (6) allows us to obtain an expression for t of the form

$$t = \eta \frac{1/c_p^* - 1}{1/c_p - 1}, \tag{7}$$

which does not depend on F_* or $E_{H\alpha}$.

Equation (7) requires the photospheric contributions c_p and c_p^* to be known. For c_p we use the values listed in Table 2 obtained for the GD model fits to observations with the narrowband filters. To obtain the corresponding values for c_p^*, we fit GD models to observations obtained without the filters (i.e., the observations obtained on 2004 December 2). The squared visibilities for the best-fit models to the 2004 December 2 data are shown in Figures 9 and 10, for γ Cas and ϕ Per, respectively. In both cases the best-fit GD model parameters (except for c_p) agree with the parameters listed in Table 2, even for γ Cas, for which we did not have enough points to constrain an elliptical model. These fits yield c_p^* values of 0.85 and 0.78 for γ Cas and ϕ Per, respectively. Using equation (7) with the appropriate values for γ Cas and ϕ Per we obtain the same estimate for t of 0.17 ± 0.01. It is interesting to note that this 17% transmission is fully consistent with the detected drop in photon counts in the Hα channel when the narrowband filters are introduced for observations of calibrator stars (which do not have Hα in emission).

TABLE 3
CIRCUMSTELLAR REGIONS OF γ Cas AND ϕ Per

Description	Symbol	γ Cas	ϕ Per
Disk size (mas)	θ_{GD}	3.59 ± 0.04	2.89 ± 0.09
Axial ratio	r	0.58 ± 0.03	0.27 ± 0.01
P.A. of major axis (deg)	ϕ	31.2 ± 1.2	-61.5 ± 0.6
Inclination (deg)...................	i	$\gtrsim 55$	$\gtrsim 74$
Half-opening angle	H_θ	$\lesssim 17$	$\lesssim 8$

Because our estimate for t does not depend on F_* or $E_{\mathrm{H}\alpha}$, we can use equation (6) to obtain a value for c_p based on spectroscopic observations. We approximate F_* with the spectral width of the Hα channel (which has been measured to be 15 ± 1 nm). To obtain the EW of the net Hα emission for ϕ Per, we use the Hα EW from § 3.2 and add a small contribution (0.37 nm) due to the absorption line that has been filled in (using the same procedure as outlined in § 4.2 of Tycner et al. 2005). The net Hα emission of 4.27 ± 0.30 nm for ϕ Per results in c_p of 0.39 ± 0.03. This estimate is significantly lower than the values listed in Table 2 for the UD and UR models, which have best-fit c_p values of 0.52 and 0.62, respectively, but it is fully consistent with the 0.39 ± 0.02 value obtained for the GD model. We interpret this as an indication that the brightness distribution of the circumstellar disk of ϕ Per is best represented by a GD model. It is interesting to note that if we follow the same reasoning for γ Cas data from the shortest two baselines (for which the degeneracy between the three models also exists), we arrive at the same conclusion that the GD model is the preferred solution. For γ Cas, based on its Hα EW of -3.1 ± 0.1 nm and an estimated component accounting for the absorption line of 0.26 nm, we estimate that $c_p = 0.45 \pm 0.03$, which again is closest to the value obtained for the GD model.

We conclude that out of the three models we have considered in our analysis, the GD model is the only model that fits γ Cas observations and is the preferred model for ϕ Per based on spectroscopic constraints. Therefore, in Table 3 we list our final best-fit parameters describing the circumstellar regions of γ Cas and ϕ Per based on the GD model fits. The model squared visibilities calculated based on these models are shown with red solid lines in Figures 7 and 8 for γ Cas and ϕ Per, respectively.

5. DISCUSSION

5.1. Circumstellar Region

Because the number of published parameters describing the circumstellar regions of γ Cas and ϕ Per is still very small, it is worthwhile to compare our results to those published in the literature. Both Quirrenbach et al. (1997) and Tycner et al. (2003) fitted a GD model to their observations, and therefore, their model values can be compared directly with those listed in Table 3.

Using observational data from the Mark III interferometer, Quirrenbach et al. (1997) obtained best-fit model parameters for γ Cas of $\theta = 3.47 \pm 0.02$ mas, $r = 0.70 \pm 0.02$, and P.A. $= 19° \pm 2°$. Tycner et al. (2003) reported results based on older NPOI observations (with a maximum baseline of 37.5 m), which had $\theta = 3.67 \pm 0.09$ mas, $r = 0.79 \pm 0.03$, and P.A. $= 32° \pm 5°$. Our new determination of the angular size of the major axis as 3.59 ± 0.04 fully confirms the previous estimates. The apparent axial ratio of 0.58 ± 0.03 that we find for γ Cas is smaller than the published values; this might be related to the fact that our interferometric observations cover a much larger range of baseline projection angles on the plane of the sky (recall Fig. 5). Our

best-fit value for the P.A. of $31°.2 \pm 1°.2$ agrees with our previous estimate (Tycner et al. 2003) but differs from the P.A. reported by Quirrenbach et al. (1997) whose value was at a right angle to the polarization vector that they obtained from polarimetry. Possible sources for this discrepancy could be the intrinsic variability of the polarization of the source (see, e.g., Table 6 in Quirrenbach et al. 1997), the residual effects associated with the removal of the interstellar polarization, or the effects of a nonaxisymmetric scattering surface (i.e., only for axisymmetric sources can one expect the polarization vector to be *exactly* perpendicular to the plane of the disk).

For ϕ Per, Quirrenbach et al. (1997) obtained model values of $\theta = 2.67 \pm 0.20$ mas, $r = 0.46 \pm 0.04$, and P.A. $= -62° \pm 5°$, but they point out that the value for r might be an upper limit because their baselines were not long enough to resolve the minor axis. Indeed, our results based on observations that use baselines that are more than twice as long as those used in their study yield a best-fit value of 0.27 ± 0.01 for the axial ratio. However, the angular size of the major axis of 2.89 ± 0.09 mas and P.A. of $-61°.5 \pm 0°.6$ that we obtain in this study fully agree with their values. Since ϕ Per was not observed by any other interferometer than Mark III, our results represent the first confirmation of the values reported by Quirrenbach et al. (1997).

5.2. Inclination and Disk Opening Angles

Our interferometric observations of the spatially resolved circumstellar regions, which show an apparent ellipticity, can be used to estimate the inclination[10] and disk opening angles. For example, if we assume that the circumstellar disk is circularly symmetric, we can obtain a lower limit on the inclination angle (i) with the observed axial ratio (r), using

$$i \gtrsim \cos^{-1} r. \qquad (8)$$

The minimum value corresponds to a geometrically thin disk, in which the entire signature of the apparent ellipticity is interpreted as a projection effect in this case. Similarly, if we assume that the geometry of the circumstellar region can be represented with a simple equatorial disk model with a half-opening angle H_θ and radius R_{disk} (see, e.g., Fig. 2 in Waters et al. 1987), we can then obtain an upper limit on H_θ using

$$H_\theta \lesssim \sin^{-1}(r/2), \qquad (9)$$

where the maximum value corresponds to a system viewed edge-on.

In Table 3 we list the estimated limits on the inclination and half-opening angles for both γ Cas and ϕ Per based on their best-fit values of r obtained from the elliptical Gaussian models. Interestingly, for ϕ Per the lower limit of $\approx 74°$ for i is consistent with the $80°$–$88°$ range originally proposed by Poeckert (1981). Although Poeckert (1981) did not describe the circumstellar region in terms of an opening angle, the disk thickness of $(1.3$–$2.7)R_*$ and the disk radius of $7.7R_*$ can be translated to a half-opening angle between $5°$ and $10°$, which again is consistent with our upper limit of $\approx 8°$.

It is instructive to compare the upper limits we obtain for H_θ of γ Cas and ϕ Per to the value of $15°$ adopted by Waters et al. (1987) in their study of almost 60 Be stars based on far-IR *IRAS* observations. Waters et al. (1987) estimated a number of different Be stellar characteristics, such as the mass-loss rate and the disk density, that had a dependence on H_θ. Although the authors

---

[10] The angle between the normal to the plane of the disk and the line of sight.

assumed an error of a factor of 1.5 in $\sin H_\theta$, our upper limit for the disk half-opening angle for ϕ Per is half their adopted value. In the case of ϕ Per, the mass-loss rate derived by Waters et al. (1987) is overestimated by at least a factor of 2, or more if the source is not viewed edge-on. Our upper limit on the half-opening angle of 17° for γ Cas is consistent with the value adopted by Waters et al. (1987). However, based on the line profile classification scheme established by Hanuschik et al. (1996) we can conclude that γ Cas is not viewed edge-on, and therefore its half-opening angle is most likely less than 17°. In the case of the Be star ζ Tau, for which the apparent ellipticity of the circumstellar region has also been detected (Quirrenbach et al. 1997; Tycner et al. 2004), one can conclude that $H_\theta \lesssim 9^\circ$. It is possible that other Be stars also have small disk opening angles. To further test the generality of this hypothesis, future interferometric observations should concentrate on systems that are thought to be viewed at large inclination angles (e.g., using the Hα profile classification of Hanuschik et al. 1996).

We can also compare our interferometrically determined opening angles with those predicted by Stee (2003), who has calculated the disk opening angles for a number of Be stars based on the flux in the Brackett continuum near 2.2 μm using the SIMECA code (Stee & de Araujo 1994; Stee et al. 1995). The main characteristic of the SIMECA model is that for a fixed disk density at the stellar photosphere, the opening angle is directly proportional to the continuum flux, so that a large flux in the K band corresponds to a large opening angle. For example, Stee (2003) obtained a value of 14° for the full opening angle of the disk of ϕ Per, which agrees with our upper value of 16°. However, our upper limit for the full opening angle for γ Cas is 34°, which is significantly less than the 54° obtained by Stee (2003) for this star. This discrepancy may be due to the fact that Stee (2003) might have used apparent and not absolute magnitudes to derive the disk opening angles, in which case the values reported in that study should be reevaluated.

5.3. Disk Truncation

Tycner et al. (2004) showed that the Hα-emitting region of the binary Be star ζ Tau was well within the estimated Roche lobe of the primary, which suggests that the disk is truncated. Another example of a possible disk truncation was presented by Chesneau et al. (2005) for α Ara, for which the Very Large Telescope Interferometer operating in the N band did not resolve any structure and therefore allowed the authors to put an upper limit on the extent of the circumstellar region. Because this limit was smaller than the expected spatial extent based on the models that were fitted to the Balmer emission lines, the authors suggest that disk truncation by an unseen companion might be occurring.

Evidence is accumulating that suggests that γ Cas is a member of a binary system. Harmanec et al. (2000) published the first orbital radial velocity curve for γ Cas based on observations collected in the 628–672 nm range from 1993 to 2000. Their analysis suggests that this star is the primary component of a spectroscopic binary with a period of ≈ 204 days and an eccentricity of 0.26. This result was confirmed by Miroshnichenko et al. (2002) using high-resolution spectroscopic observations of the Hα line obtained over a similar time period. They report a periodic change of 205 days in this line, which they also attribute to the binary system. Although Harmanec et al. (2000) conclude that the secondary could be either a hot compact object or a low-luminosity late-type star, they estimate that the separation between the components at periastron could be between 250 and 300 $R_\odot$. The distance to γ Cas is 188 ± 20 pc based on *Hipparcos* satellite measurements (Perryman et al. 1997), which places the separa-

tion between the components at 6.2–7.4 mas. Our best-fit value for the FWHM of the major axis is 3.59 ± 0.04, and therefore, the circumstellar disk is well within the orbit established by Harmanec et al. (2000). However, because the binary parameters of γ Cas are not well established this comparison is tentative.

The binary nature of ϕ Per is much better established, since it was recognized as a binary in the early 1900s (Cannon 1910; Ludendorff 1911). Poeckert (1981) documents the development in the understanding of ϕ Per's binary nature over the succeeding decades, and suggests that a subdwarf O star is the secondary. Gies et al. (1998) detected the secondary in ultraviolet spectra obtained with the *Hubble Space Telescope* and confirmed Poeckert's prediction. Along with HR 2142 (Waters et al. 1991), 59 Cyg (Maintz 2003), and FY CMa (Rivinius et al. 2004), ϕ Per is now part of a group of four candidate Be+sdO binaries. Be+sdO binaries may result from a spin-up of the B star as a result of mass transfer from the progenitor of the evolved subdwarf companion.

Estimates of the orbital parameters of ϕ Per are available in Božić et al. (1995) and Gies et al. (1998). The semimajor axes of these two orbital solutions range from approximately 230 to 310 $R_\odot$. Using the *Hipparcos* distance of 220^{+43}_{-31} pc for ϕ Per (Perryman et al. 1997), we expect an angular separation of 4.9–6.6 mas between the components of ϕ Per. As we would expect, this separation is larger than the angular radius of any of the models of ϕ Per listed in Table 2. The radial extent of the Gaussian model can be approximated with the FWHM measure of 3.12 ± 0.08 mas ($148 \pm 30 R_\odot$) we obtain for ϕ Per (i.e., assuming that the radial extent is twice the half-width of the Gaussian). This disk radius is very close to the 178–204 $R_\odot$ Roche radius of the primary obtained by Božić et al. (1995). This is most likely another example of a Hα-emitting region that is close in size to the actual extent of the circumstellar region, and this suggests that disk truncation is occurring in this system.

We should note that in the case of ϕ Per the presence of a truncated disk has been predicted. Waters (1986) used the *IRAS* observations of ϕ Per at 12, 25, and 60 μm to measure the IR excess and constrained the density distribution of $\rho(R) = \rho_o(r/R_*)^{-n}$ with $n = 3.1$ for the disk model. Because he obtained a value of $n = 2.4$ for two other Be stars, δ Cen and χ Oph, which also happens to correspond to a velocity law that has a more gradual increase with distance (something that is predicted based on the Hα spectroscopy), he argued that a density distribution with $n = 2.4$ might be more appropriate for ϕ Per, which could be only satisfied if the disk model was truncated at $\sim 6.5 R_*$ (or $\sim 46 R_\odot$). The apparent discrepancy between our values for the size of the truncated disk might be related to the different wavelength regimes of our studies, as well as to the assumption made by Waters (1986) that the system is viewed pole-on, whereas i might be very close to 90°.

Poeckert (1981) also predicted a second Hα-emitting disk associated with the secondary component. Although our V^2 data in the Hα channel do not have a very high S/N, we do not detect any deviations from the elliptical Gaussian model that would suggest a binary signature in the Hα signal. Therefore, we are forced to conclude that if the secondary star does possess a Hα-emitting disk it does not contribute significantly to the net Hα emission line. This is also consistent with the secondary's disk radius of 6–8 $R_\odot$ estimated by Božić et al. (1995) based on the peak separation of the He II emission line. Assuming that the Hα emission is proportional to the area of the disk, as demonstrated by Tycner et al. (2005), we conclude that the Hα emission from the disk of the secondary contributes less than $\sim 1\%$ to the total Hα flux.

The direct detection of the secondary with the NPOI is unlikely as Gies et al. (1998) report a brightness ratio of 0.15 (or

Δm of 2) at 164.7 nm. The NPOI operates over a bandwidth of 550–850 nm, and at these wavelengths the magnitude difference between the two components is likely to be much larger than 2. A search for a binary signature (a sinusoidal variation) across the continuum channels in both γ Cas and ϕ Per yielded null results. On the other hand, a binary signature with a small V^2 amplitude (less than $\sim$3%) could not be ruled out. In fact, it might be possible to detect the signature of binarity in both stars at longer wavelengths, since γ Cas may be associated with a cool companion and ϕ Per might contain larger contributions from the circumstellar disks of both components due to free-free and free-bound emission.

6. CONCLUSIONS

We have successfully demonstrated the use of a narrowband filter in the NPOI to increase the contrast between the Hα-emitting material and the central star. Our observations of two Be stars, γ Cas and ϕ Per, and our subsequent analysis have yielded the following results:

1. We have demonstrated that the uniform disk or ringlike models are inconsistent with the observations of the circumstellar region of γ Cas, whereas a Gaussian model is fully consistent with the data. However, since the thermal structure of the circumstellar disks of Be stars can be quite complex, as suggested by recent models (Millar & Marlborough 1998; Carciofi & Bjorkman 2006), it might turn out that a more complicated brightness distribution may be required to fully describe these regions.

2. The circumstellar disk of γ Cas appears to be consistent with the orbital parameters published in the literature. However, higher precision binary solutions are required to test for the possible disk truncation by the secondary.

3. Based on interferometric and spectroscopic data we have shown that the brightness distribution of the Hα-emitting circumstellar region of ϕ Per is best represented by a Gaussian distribution.

4. Our analysis supports the earlier prediction by Waters (1986) that the disk of ϕ Per is truncated due to the presence of an orbiting companion. However, the disk size we report is different than the value determined by Waters (1986). This discrepancy is likely due to different wavelength regimes used in each study and/or due to the low inclination angle assumed by Waters (1986) for this star, whereas we obtain $i \gtrsim 74°$.

A natural extension of the analysis presented in this study is the direct comparison of interferometric data with theoretically predicted interferometric observables, such as synthetic squared visibilities. Future observations and modeling are planned that combine narrowband interferometry with spectroscopy for several other Be stars, especially those that possess weak Hα emission. The goal of this work is to place greater constraints on the spatial extent and physical properties of the circumstellar material. These constraints will allow various dynamical models to be tested with greater certainty.

REFERENCES

Armstrong, J. T., et al. 1998, ApJ, 496, 550
Barnes, T. G., Evans, D. S., & Moffett, T. J. 1978, MNRAS, 183, 285
Berio, P., et al. 1999, A&A, 345, 203
Božić, H., et al. 1995, A&A, 304, 235
Cannon, J. B. 1910, JRASC, 4, 195
Carciofi, A. C., & Bjorkman, J. E. 2006, ApJ, 639, 1081
Chesneau, O., et al. 2005, A&A, 435, 275
Gies, D. R., et al. 1998, ApJ, 493, 440
Hall, J. C., Fulton, E. E., Huenemoerder, D. P., Welty, A. D., & Neff, J. E. 1994, PASP, 106, 315
Hanuschik, R. W., Hummel, W., Sutorius, E., Dietle, O., & Thimm, G. 1996, A&AS, 116, 309
Harmanec, P., et al. 2000, A&A, 364, L85
Hummel, C. A., et al. 2003, AJ, 125, 2630
Ludendorff, H. 1911, Astron. Nachr., 186, 17
Maintz, M. 2003, Ph.D. thesis, Univ. Heidelberg
Millar, C. E., & Marlborough, J. M. 1998, ApJ, 494, 715
Millar, C. E., Sigut, T. A. A., & Marlborough, J. M. 2000, MNRAS, 312, 465
Miroshnichenko, A. S., Bjorkman, K. S., & Krugov, V. D. 2002, PASP, 114, 1226
Pauls, T. A., Gilbreath, G. C., Armstrong, J. T., Mozurkewich, D., Benson, J. A., & Hindsley, R. B. 2001, BAAS, 33, 861
Perryman, M. A. C., et al. 1997, A&A, 323, L49
Poeckert, R. 1981, PASP, 93, 297

Press, W. H., Teukolsky, S. A., Vetterling, W. T., & Flannery, B. P. 1992, Numerical Recipes in C (2nd ed.; Cambridge: Cambridge Univ. Press)
Quirrenbach, A., et al. 1997, ApJ, 479, 477
Rivinius, T., Štefl, S., Maintz, M., Stahl, O., & Baade, D. 2004, A&A, 427, 307
Schmitt, H. R., Armstrong, J. T., Hindsley, R. B., & Pauls, T. A. 2005, BAAS, 206, 15.01
Stee, P. 2003, A&A, 403, 1023
Stee, P., & de Araujo, F. X. 1994, A&A, 292, 221
Stee, P., de Araujo, F. X., Vakili, F., Mourard, D., Arnold, L., Bonneau, D., Morand, F., & Tallon-Bosc, I. 1995, A&A, 300, 219
Thompson, A. R., Moran, J. M., & Swenson, G. W. 2001, Interferometry and Synthesis in Radio Astronomy (2nd ed.; New York: Wiley-Interscience)
Tycner, C., et al. 2003, AJ, 125, 3378
———. 2004, AJ, 127, 1194
———. 2005, ApJ, 624, 359
Underhill, A. B., Divan, L., Prevot-Burnichon, M.-L., & Doazan, V. 1979, MNRAS, 189, 601
Vakili, F., et al. 1998, A&A, 335, 261
van Belle, G. T. 1999, PASP, 111, 1515
Waters, L. B. F. M. 1986, A&A, 162, 121
Waters, L. B. F. M., Coté, J., & Lamers, H. J. G. L. M. 1987, A&A, 185, 206
Waters, L. B. F. M., Coté, J., & Pols, O. R. 1991, A&A, 250, 437
Wittkowski, M., et al. 2001, A&A, 377, 981
Wood, K., Bjorkman, K. S., & Bjorkman, J. E. 1997, ApJ, 477, 926